The Astrophysical Journal, 945:58 (15pp), 2023 March 1 https://doi.org/10.3847/1538-4357/acb701

Synthesizing Spectra from 3D Radiation Hydrodynamic Models of Massive Stars Using Monte Carlo Radiation Transport

William C. Schultz[1], Benny T.-H. Tsang[2], Lars Bildsten[1,3], and Yan-Fei Jiang (姜燕飞)[4]
[1] Department of Physics, University of California, Santa Barbara, CA 93106, USA; wcschultz@physics.ucsb.edu
[2] Department of Astronomy and Theoretical Astrophysics Center, University of California, Berkeley, CA 94720, USA
[3] Kavli Institute for Theoretical Physics, University of California, Santa Barbara, CA 93106, USA
[4] Center for Computational Astrophysics, Flatiron Institute, New York, NY 10010, USA
Received 2022 September 27; revised 2022 December 20; accepted 2023 January 28; published 2023 March 7

Abstract

Observations indicate that turbulent motions are present on most massive star surfaces. Starting from the observed phenomena of spectral lines with widths that are much larger than their thermal broadening (e.g., micro- and macroturbulence), and considering the detection of stochastic low-frequency variability (SLFV) in the Transiting Exoplanet Survey Satellite photometry, these stars clearly have large-scale turbulent motions on their surfaces. The cause of this turbulence is debated, with near-surface convection zones, core internal gravity waves, and wind variability being proposed. Our 3D gray radiation hydrodynamic (RHD) models previously characterized the convective dynamics of the surfaces, driven by near-surface convection zones, and provided reasonable matches to the observed SLFV of the most luminous massive stars. We now explore the complex emitting surfaces of these 3D RHD models, which strongly violate the 1D assumption of a plane-parallel atmosphere. By post-processing the gray RHD models with the Monte Carlo radiation transport code SEDONA, we synthesize stellar spectra and extract information from the broadening of individual photospheric lines. The use of SEDONA enables the calculation of the viewing angle and temporal dependence of spectral absorption line profiles. By combining uncorrelated temporal snapshots together, we compare the turbulent broadening from the 3D RHD models to the thermal broadening of the extended emitting region, showing that our synthesized spectral lines closely resemble the observed macroturbulent broadening from similarly luminous stars. More generally, the new techniques that we have developed will allow for systematic studies of the origins of turbulent velocity broadening from any future 3D simulations.

Unified Astronomy Thesaurus concepts: Astrophysical fluid dynamics (101); Hydrodynamics (1963); Computational methods (1965); Radiative transfer simulations (1967); Stellar spectral lines (1630); Stellar convection envelopes (299)

1. Introduction

Observations of massive stars exhibit clear signs of highly turbulent surfaces. The Transiting Exoplanet Survey Satellite (Ricker et al. 2015) has observed many O and B stars and found that nearly all exhibit brightening variations at low frequencies, $\nu \lesssim 10^{-4}$ Hz, or 10 cycles per day (Bowman et al. 2019; Burssens et al. 2020). This phenomenon is termed stochastic low-frequency variability (SLFV) and it is thought to be produced by large-scale turbulent motions. The physical mechanism that generates this SLFV could have several origins: turbulent plumes from near-surface convection zones (Cantiello et al. 2021; Schultz et al. 2022), internal gravity waves (IGWs) launched from the convective core (Aerts & Rogers 2015; Edelmann et al. 2019), or wind variability and dynamics (Krtička & Feldmeier 2021). Though near-surface convection zones appear to generate similar trends to the observed SLFV strength and characteristic frequency (Cantiello et al. 2021; Schultz et al. 2022), the question still remains worthy of exploration across the Hertzsprung–Russell diagram. Additionally, Schultz et al. (2022) have found the photospheric velocities seen in 3D models are comparable to the observed spectroscopic broadening of similar stars.

Analyzing spectral lines from these massive stars provides a distinct additional probe, as photospheric spectral lines are broadened by the velocity fields in the emitting regions. The analysis of 2D models by Rogers et al. (2013) has suggested that IGWs could generate photospheric spectral line variability that could be observable by future surveys (Aerts & Rogers 2015). However, full 3D frequency-dependent radiation hydrodynamic (RHD) models have not been computed, and are challenging with current computing power.

To understand how spectral line broadening provides local velocity information, we look to previous methods of modeling lower-mass stellar spectra (Gray 2005). Typically, four main velocities are used to fit photospheric spectral lines. Thermal broadening comes from the intrinsic Maxwell–Boltzmann velocity distribution of the ions, $v_{\rm therm}$, and is Gaussian in profile. This is often combined with intrinsic broadening, which arises from the atomic physics governing the line-level transitions, to generate a Voigt profile for the spectral line. Projected rotational broadening, $v \sin i$, imparts a steep deep walled trench shape on stellar spectral lines, as half the star is redshifted while the other half is blueshifted.

The other two velocities arise from the impacts of turbulent motions in the line-forming regions. The microturbulent velocity, denoted as ξ, accounts for the additional velocities impacting scales smaller than the emitting region, and is added in quadrature to $v_{\rm therm}$ in the Gaussian broadening of spectral lines. In this work, the emitting region is defined as the volume

where the photons experience their final interactions before leaving the stellar atmosphere, and it is typically similar to the scale height near the photosphere. As ξ affects the equivalent width, it is typically quantified using Curve of Growth analyses of heavy elements for which $\xi \gg v_{\rm therm}$. The other turbulent broadening arises from macroturbulence, $v_{\rm macro}$, which corresponds to dynamics on scales larger than the emitting region. This broadens the wings of the spectral lines and is typically used as a fitting parameter, as discussed in Gray (2005).

Though these velocity choices have been inherited from investigations of lower-mass stars, they are very effective in fitting the spectral lines of hot massive stars (Simón-Díaz et al. 2010, 2014, 2017, 2018; Holgado et al. 2022). However, because the turbulent surfaces of massive stars are significantly different to those of their low-mass counterparts (Jiang et al. 2018; Schultz et al. 2020, 2022), it is uncertain just how accurate the inferred ξ and $v_{\rm macro}$ will be, based on the existing line-fitting approach. One example of an unexplained discrepancy is the strong positive correlation between $v \sin i$ and $v_{\rm macro}$ for massive stars ($M > 20\,M_{\odot}$) across the main sequence (Simón-Díaz et al. 2017). Additionally, when using the current fitting method, a larger ξ appears to limit the range of recoverable $v \sin i$ and $v_{\rm macro}$ (Simón-Díaz et al. 2014), implying that both a quantification of these broadening velocities, as well as a better theoretical understanding of their meanings for turbulent massive star surfaces, are needed.

Additionally, the violent turbulent plume structures on the surfaces of these massive stars suggest that 1D spectral synthesis models (e.g., FASTWIND—Santolaya-Rey et al. 1997) may be insufficient. 3D RHD models present a more realistic method of probing their chaotic surface dynamics, where the interplay between radiation and matter is taken into account in the excitation of the turbulence. Similar investigations (see Dravins et al. 2021 and references therein) have been performed for lower-mass (F, G, and K) stars, where the gas pressure dominates radiation and the velocities are subsonic, allowing 3D hydrodynamic models to be used without the need for radiation pressure. These hydro models have then been post-processed with radiation transport, to synthesize stellar spectra with good agreement. Similar work with RHD models has been done for red supergiants (RSGs), with radiation becoming an important source of pressure support near the surface (Chiavassa et al. 2011). Using the 3D radiation transport code OPTIM3D, Chiavassa et al. (2009) post-processed their CO^{5}BOLD (Freytag et al. 2002; Freytag & Höfner 2008) RHD models, using tabulated extinction coefficients specific to the T and ρ of RSG surfaces, to generate spectra over a wide frequency range.

For hotter massive star envelopes, the problem requires more computational resources, as the entire envelopes are supported by the interplay between plasma, radiation, and turbulence. Near-surface convection zones excited by near-Eddington luminosities traveling through opacity peaks lead to turbulent dynamics and inefficient convection, as the motions become transonic and the optical depths are low enough that rising plumes can lose heat from radiative cooling (Goldberg et al. 2022; Schultz et al. 2022). Fortunately, this physics is within the reach of our 3D gray RHD simulations, which have been run using ATHENA++ (Stone et al. 2020), and we can now post-process them for the desired spectroscopic analysis.

We choose to post-process our ATHENA++ models using SEDONA, a Monte Carlo (MC) radiation transport framework that was originally developed to model supernova light curves, spectra, and polarization (Kasen et al. 2006). SEDONA calculates frequency-dependent opacities directly from the atomic data in the comoving frame of each cell, without the need for the Sobolev or line expansion approximations, allowing for generic applications to a wide range of stellar envelopes, with adjustable frequency resolution. Additionally, the MC transport is beneficial, as it directly tracks the transport paths of the photons through the clumpy and dynamic plume structures, and can be used to estimate the viewing angle dependencies from 3D simulations. Though it is not used in this analysis, SEDONA will allow for future expansions of this work: exploring the polarization of the emitted flux, comparing gray and non-gray radiation transport, and comparing local thermal equilibrium (LTE) and non-LTE calculations in investigations of wind lines. Two major modifications to SEDONA were necessary to adapt it to massive star surfaces. A 3D spherical wedge geometry, matching that of our ATHENA++ simulations, was added so that we were able to initialize our models in the SEDONA framework. Additionally, a novel emission method was developed to avoid transporting MC particles (MCPs) through excessively optically thick zones. Detailed discussions of these modifications are presented in Section 3.

Generating synthetic spectral lines from a turbulent stellar surface is nontrivial. Forests of lines and ionization changes cause the stellar atmosphere to become more opaque, with its average resulting in the Fe and He opacity peaks seen in gray opacities. This leads to stronger radiation forces on these opaque fluid parcels, which rise until they diffuse enough for the radiation to pass through them. Due to the strong radiation field of these nearly Eddington-limited atmospheres, the fluid parcels accelerate to transonic speed and collide with adjacent plasma, generating turbulence. To accurately model the RHD of this turbulent medium, including the thermal background as well as the strong narrow lines, a wide frequency range and a high frequency resolution are both needed, which drive up the computational costs significantly. Additionally, the nearly Eddington-limited radiation field and the ρ fluctuations from the transonic turbulence combine to launch plumes from the stellar surface, creating dynamic emitting regions for the spectral lines, which are starkly different to those in 1D atmospheric models. This strong turbulence also generates large velocity contrasts, broadening the lines ($\Delta\lambda \sim 5$ Å) to create line blending, which is not expected in static models.

In this work, we present our method for post-processing 3D models to synthesize stellar spectra. The 3D gray RHD simulations used for post-processing are described in Section 2, which specifically presents the model parameters for the three models investigated and a comparison of the photosphere versus $\tau = 1$ surfaces in the models. In Section 3, we detail the MC radiation transport methods and compare the gray transport between the simulations. We describe the process of synthesizing the spectral lines in Section 4, as well as that of depicting the variety in the emitting regions of the individual lines in the models. In Section 5, we highlight the results for one spectral line from each model and compare the impacts of $v_{\rm therm}$ and the velocity fields of the models, predicting implications for ξ and $v_{\rm macro}$. We conclude with a brief summary of the future work that these new methods will allow in Section 6.

Table 1
Properties of the 3D Stellar Models

Name	Masses		Temperatures		Luminosities		Resolution	Angular Size	
	$M_{\rm core}$ ($M_\odot$)	$M_{\rm env}$ ($M_\odot$)	$T_{{\rm eff},F_{\rm r}}$[a] (10^3 K)	$T_{\rm eff}$[b] (10^3 K)	L ($\log(L/L_\odot)$)	$L_{\rm Edd}$[c] ($\log(L/L_\odot)$)	$n_{\rm r}$, n_θ, n_ϕ	$\theta_{\rm min}$, $\theta_{\rm max}$ | $\phi_{\rm min}$, $\phi_{\rm max}$ (π, π | π, π)	$\Omega_{\rm sim}$ (sr/π)
T19L6.4	80	0.011	25	19	6.4	6.42	512, 256, 512	0.25, 0.75 | 0, 1	1.41
T32L5.2	35	10^{-4}	35	32	5.2	6.07	336, 256, 256	0.44, 0.56 | 0, 0.11	0.04
T42L5.0	35	10^{-6}	42	42	5.0	6.07	384, 128, 128	0.49, 0.51 | 0, 0.02	0.0012

Name	Radii					Optical Depth		rms Velocities		Scale Heights	
	$r_{\rm base}$ ($R_\odot$)	$r_{\rm Fe}$ ($R_\odot$)	$r_{F_{\rm r}=\sigma T^4}$[d] ($R_\odot$)	$r_{\tau=1}$[e] ($R_\odot$)	$r_{\rm max}$ ($R_\odot$)	$\tau_{\rm Fe}$	$\frac{\tau_{\rm Fe}}{\tau_{\rm crit}}$	$v_{{\rm r},\tau=1}$ (km s^{-1})	$v_{\perp,\tau=1}$ (km s^{-1})	$H_{\rm Fe}$ ($R_\odot$)	$H_{\tau=1}$ ($R_\odot$)
T19L6.4	16.3	44.0	78.6	99.1	335.5	5,200	2.5	120	95	4.36	13.2
T32L5.2	9.7	12.5	13.07	13.15	15.3	1,182	0.28	68	78	0.24	0.09
T42L5.0	6.8	7.7	7.86	7.86	8.2	490	0.02	2.5	8.6	0.07	0.01

Notes. Note that T32L5.2 is the same model as T35L5.2 in Schultz et al. (2022), as a different $T_{\rm eff}$ definition was used.
[a] Defined as the angle-averaged temperature at $r_{F_{\rm r}=\sigma T^4}$ ($\langle T(r_{F_{\rm r}=\sigma T^4})\rangle$).
[b] Defined as the angle-averaged temperature at $r_{\tau=1}$.
[c] For an assumed electron-scattering opacity.
[d] Defined as the radius where the angle-averaged radiative flux follows the Stefan–Boltzmann law ($\langle F_{\rm r}(r_{F_{\rm r}=\sigma T^4})\rangle = \sigma\langle T(r_{F_{\rm r}=\sigma T^4})\rangle^4$).
[e] Defined as the radius where the angle-averaged optical depth is unity ($\langle\tau(r_{\tau=1})\rangle = 1$).

2. 3D Gray RHD Modeling

A number of 3D gray RHD models have simulated near-surface convection zones in massive star envelopes (Jiang et al. 2015, 2018; Schultz et al. 2022). These models have been performed using ATHENA++ (Stone et al. 2020) and additional radiation transport (Jiang et al. 2012, 2014; Jiang 2021). In this work, we showcase our novel spectral synthesis software pipeline by post-processing three specific ATHENA++ models from the simulation suite. In Section 2.1, we briefly summarize the numerical treatments and the stellar properties of the envelope models. We then explain how the common interpretation of having the photosphere at a constant radius is incomplete, in Section 2.2, before introducing the thermalization optical depth as a reliable basis for estimating where spectral features are formed and exploring what these surfaces look like in our 3D models, in Section 2.2.1.

2.1. ATHENA++ Model Description

The ATHENA++ stellar envelope models are run on spherical polar grids and use an HLLC Riemann solver for the hydrodynamics. The radiation transport equation is solved implicitly, using discrete ordinates and assuming LTE, following Jiang (2021). In our model suite, the finite-volume approach of radiation transport discretizes the radiation field of each cell into 120 angular directions over the full 4π solid angle. The gravitational acceleration follows $g \propto M_{\rm core}/r^2$, not including the self-gravity of the envelope, as the envelope masses within the models, $M_{\rm env}$, are <0.1% of the core mass, $M_{\rm core}$. Rotation and magnetic fields are omitted from these models, as they are not expected to significantly affect the near-surface opacity peaks or the turbulence that they excite (Jiang et al. 2017; Cantiello et al. 2021; Schultz et al. 2022). As the ionization states of the plasma do not drastically affect the equation of state in stellar atmospheres with $T_{\rm eff} \gtrsim 10{,}000$ K, constant solar mean molecular weights are used in these models. These models utilize gray OPAL Rosseland mean opacities (Iglesias & Rogers 1996) at solar composition, in a fully ionized plasma. The gray opacity approximation and the LTE assumption likely break down outside the stellar surface, where the continuum opacity falls below the atomic line opacity. Thus, our analysis is limited to photospheric spectral lines.

The ATHENA++ stellar envelope model parameters for the simulations used here are summarized in Table 1. The models are named by their $T_{\rm eff}/10^3$ K and $\log(L/L_\odot)$, and they simulate the outer convective regions between boundary radii from $r_{\rm base}$ to $r_{\rm max}$. Because the pressure scale height ($H \equiv P/\rho g$) is much smaller than the radial extent in these stars ($H \ll R$, in Table 1), only a small spherical wedge is modeled over a limited solid angle ($\Omega_{\rm sim} < 4\pi$), to limit the computational costs. The size of each wedge has been chosen such that it would include at least 10 scale heights in the angular dimensions at the location of the Fe opacity peak, i.e., $(\phi_{\rm max} - \phi_{\rm min}) \times r_{\rm Fe} \geqslant 10\,H_{\rm Fe}$. The radial refinement is set to $\delta r/r \lesssim 0.1\%$ and the angular resolution ensures $r\delta\theta \approx r\delta\phi \approx \delta r$. This allows each model to capture approximately five convective plumes, each more than 30 model cells across. The θ extent of each simulation domain is centered on π, to alleviate numerical problems at the poles. The inner boundary condition fixes T, ρ, $F_{\rm r}$, and $v_{\rm r} = v_\perp = 0$ in the radiative region between the core and modeled regions, while the outer boundary is open, to allow radiation to escape and possible outflows. The angular boundaries along the θ and ϕ directions are periodic.

The ATHENA++ models are initialized using 1D models from the Modules for Experiments in Stellar Astrophysics (MESA; Paxton et al. 2011, 2013, 2015, 2018, 2019; Jermyn et al. 2022), using the default inlists. The T, ρ, and r at the Fe opacity peak in the MESA models are used with the M and L to create a hydrostatic model that is in thermal equilibrium without any convection, which initializes the 3D simulations. The outer regions of the simulation, outside the stellar profile, are initialized with a low-density floor ($\rho = 10^{-17}$ g cm^{-3}), to allow the models to find equilibrium without affecting the envelope mass, resulting in an integrated optical depth, $\tau_{\rm floor} \approx 10^{-6}$. When the ATHENA++ run begins, the initial solution is unstable to convective motion and near-surface

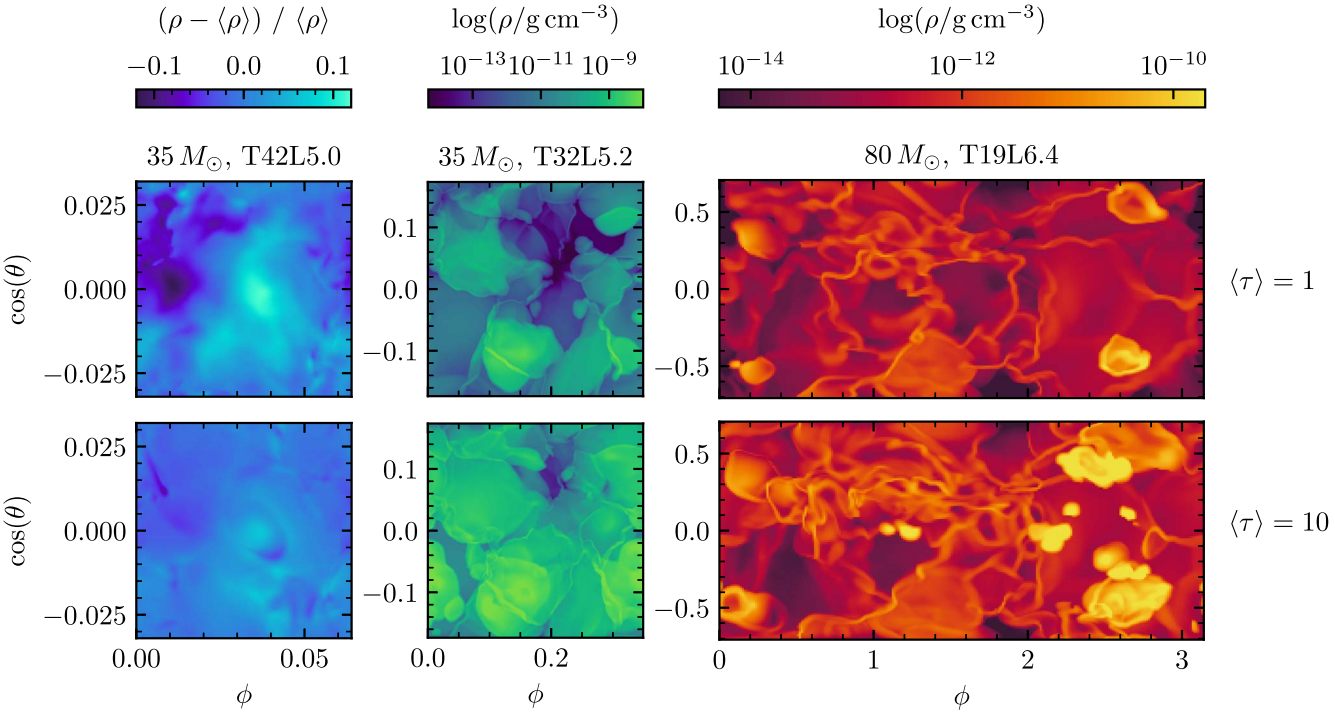

Figure 1. Density fluctuations through a slice at constant radius, where the angle-averaged optical depth, $\langle\tau\rangle$, is 1 (top) and 10 (bottom), for T42L5.0, T32L5.2, and T19L6.4 (left to right). The colors show the over- and underdensities in the left column and $\log\rho$ in the middle and right columns.

convection zones develop. The models are run until the time-averaged radial energy flux has converged and the Fe opacity peak has experienced at least three thermal times, $t_{\rm therm} = \int_{r_{\rm Fe}}^{r_{\rm max}} C_{\rm P} T \Big/ LdM$, where $C_{\rm P}$ is the heat capacity at constant pressure. Once these conditions have been met, typically after $\gtrsim 10^7$ core hours, we are satisfied that steady-state equilibrium has been reached.

All these models are of hot bright stars, with T19L6.4 in the Hertzsprung gap, T32L5.2 in the middle of main-sequence evolution, and T42L5.0 near the zero-age main sequence. Their luminosities are nearly Eddington-limited for an electron-scattering opacity, $L \sim L_{\rm Edd} \equiv 4\pi GMc/\kappa_{\rm es}$, and thus any increase in opacity from the prevailing Fe and He opacity peaks will cause vigorous convective dynamics. These convective zones are best understood by quantifying their convective efficiency using an optical depth diagnostic. In optically thick convection zones, the convective efficiency can be written as the advective flux over the diffusive radiative flux, or approximately $\gamma = (P_{\rm r} + P_{\rm g}) v_{\rm conv}/P_{\rm r}(c/\tau)$, where $v_{\rm conv}$ is the convective velocity and $P_{\rm r}$ and $P_{\rm g}$ are the radiation and gas pressures, respectively. We solve for an optical depth at which $\gamma = 1$, or the point at which both transport methods are equal, to define $\tau_{\rm crit}$:

$$\tau_{\rm crit} \equiv \frac{cP_{\rm r}}{v_{\rm rms}(P_{\rm r} + P_{\rm g})}, \tag{1}$$

where we have assumed that the convective velocity is similar to the rms velocity, $v_{\rm conv} \approx v_{\rm rms}$ (Jiang et al. 2015; Schultz et al. 2020; Goldberg et al. 2022). Thus, if a convective zone lies at $\tau > \tau_{\rm crit}$, we expect the convective energy transport to dominate there. Otherwise, though still convective, the majority of the luminosity is carried via radiative diffusion in the turbulent medium. Looking at $\tau_{\rm Fe}/\tau_{\rm crit}$ in Table 1, it is clear that T42L5.0 will have much less efficient convection in the Fe opacity peak convection zone, and thus weaker surface turbulence. Following the same logic, we expect T19L6.4 to have the strongest convection and fastest velocity fields, while T32L5.2 is somewhere in the middle. Comparing the surface velocities ($v_{{\rm r},\tau=1}$ and $v_{\perp,\tau=1}$), we confirm this to be the case, with T19L6.4 having the strongest velocity field and T42L5.0 having the weakest.

2.2. Photospheric Definition for a Clumpy Surface

All our 3D RHD models, independent of θ and ϕ, lack the conventional manifestation of a photosphere at a constant radius. The 3D analog to a 1D model photosphere would involve identifying the location where the angle-averaged optical depth is unity ($r_{\tau=1}$; see Table 1). However, individual line-of-sight (e.g., along specific θ, ϕ) optical depths can differ significantly when near-surface convection is vigorous. Additionally, a second photospheric definition, the location where the angle-averaged radiation field follows the Stefan–Boltzmann law ($r_{F_{\rm r}=\sigma T^4}$; see Table 1), also disagrees with $r_{\tau=1}$ by roughly a pressure scale height in the 3D models, when the turbulence is strong. Transonic velocity fields, generated by the Fe and He opacity peaks near the surface (Jiang et al. 2015, 2018; Schultz et al. 2020, 2022), create large density contrasts ($\rho/\langle\rho\rangle \gtrsim 100$) over a relatively narrow temperature range ($T/\langle T\rangle \lesssim 1$). As opacity is very sensitive to density in these opacity peak regions, any overdensity would strongly modify the local heat transport. The complex topography of the photosphere is also characteristic for constant-τ surfaces for $\tau \gtrsim 100$.

Figure 1 shows the ρ variations across slices of constant radius, or radial slices, at two choices of integrated volume-weighted, angle-averaged optical depth, $\langle\tau\rangle = 1$ and $\langle\tau\rangle = 10$. The optical depth is integrated along radial lines of sight, lines of constant (θ, ϕ), from the outer boundary of the simulation

domain to the cell, then angle-averaged to calculate $\langle\tau\rangle$. In T42L5.0, the density only deviates from the mean by less than 12% at $\langle\tau\rangle = 1$, as the turbulent velocities are small and subsonic. In contrast, T32L5.2 and T19L6.4 contain ρ values spanning more than four orders of magnitude at single radial locations, resulting from the transonic turbulence at both $\langle\tau\rangle = 1$ and $\langle\tau\rangle = 10$. As $\langle\tau\rangle$ is approximately the optical depth of the deepest cell, and $\tau_{\rm cell} \approx \kappa\rho\delta r$, the large ρ contrasts with the comparatively small changes in κ and δr, resulting in optical depth variations of $\tau \sim 0.1$–1000 along these radial slices. Defining a single radius where the angle-averaged optical depth equals a chosen constant is therefore not a reliable approximation for the photosphere. Instead, we found that surfaces of constant thermalization optical depth, which can span several scale heights, are the more realistic representation of the local photosphere.

2.2.1. Thermalization Optical Depth Surfaces

The identification of the line-emitting region is paramount for establishing a physical understanding of the velocity broadening seen in the synthetic spectral lines. Thus, instead of looking at $\tau(r) \equiv \int_r^\infty \kappa(r')\rho(r')dr'$, where $\kappa(r')$ is the total opacity, dividing the opacity into absorption and scattering components, $\kappa_{\rm a}$ and $\kappa_{\rm s}$, respectively, performing the mean free path analysis results in the thermalization optical depth (also known as the effective optical depth; see Section 1.7 of Rybicki & Lightman 1979):

$$\tau_{\rm th} \equiv \int_r^\infty \sqrt{\kappa_{\rm a}(r')(\kappa_{\rm a}(r') + \kappa_{\rm s}(r'))}\,\rho(r')dr'. \quad (2)$$

This defines the optical depth with regard to creation events (via thermalization) of the photons, rather than the location of the last scattering. We can estimate the typical number of emission and absorption events using $N \approx \tau_{\rm th}^2$. The condition $\tau_{\rm th} = 1$ thus characterizes the regions where the photons are created.

To identify the surface along $\tau_{\rm th} = 1$, Equation (2) is integrated from the outer edge of the simulation domain to the local radius, along fixed (θ, ϕ) radial lines of sight. The contribution of the low-density floor material ($\rho = 10^{-17}$ g cm^{-3}) to the optical depth is small ($\tau_{\rm floor} \approx 10^{-5}$), and is ignored. We identify the outermost cell that contains the location of the integrated $\tau_{\rm th} = 1$, referred to as the thermalization cell (TC). A schematic diagram of this integration process, to accumulate $\tau_{\rm th}$ inward to a given value, $\tau_{\rm spec}$, as well as the definition of the TCs, is depicted in Figure 2.

Figure 3 compares the variety of $\tau_{\rm th}$ when integrating to the tops (dashed lines) and bottoms (solid lines) of the TCs in the T32L5.2 model. Integrating to the tops of the TCs, 10% of the lines of sight see significantly lower thermalization optical depths, whereas including the entirety of the TCs results in 10% of the lines of sight seeing twice the expected $\tau_{\rm th}$. The variety along the same $\tau_{\rm th} = 1$ surfaces in the other two models is comparable to that of Figure 3.

The large variety of $\tau_{\rm th}$ in the adjacent cells is created by the turbulent structure. Infalling material, previously ejected from earlier plumes penetrating the surface, collides with rising plumes, creating shocks and thus large density contrasts. These density contrasts are responsible for the significantly higher $\tau_{\rm th}$ along many of the $\tau_{\rm th} = 1$ surfaces (solid green line in Figure 3).

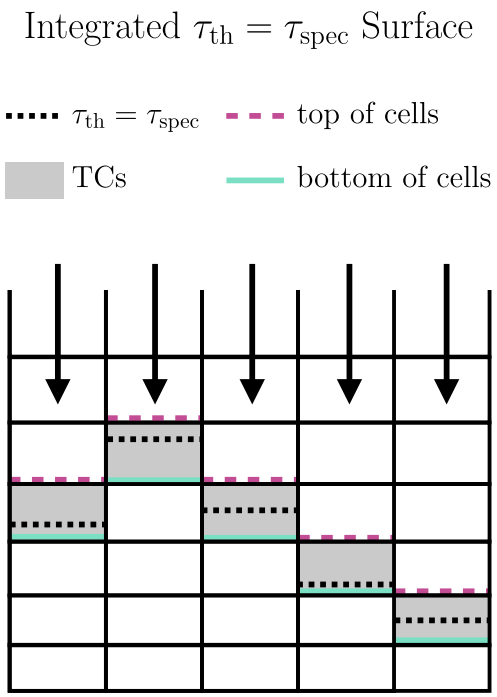

Figure 2. Schematic of the constant (θ, ϕ) integration process for integrated $\tau_{\rm th} = \tau_{\rm spec}$ surfaces, where $\tau_{\rm spec}$ is the desired value for $\tau_{\rm th}$. The dotted black lines depict the locations along each radial line of sight where $\tau_{\rm th}$ is equal to the desired value, while the dashed pink and solid cyan lines show the tops and bottoms, respectively, of the cells in which the equality is met. The cells themselves, referred to as TCs, are shaded in gray.

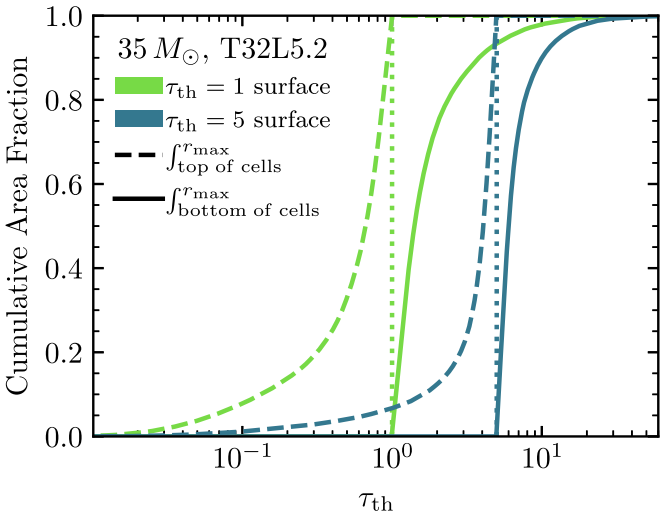

Figure 3. Variety in the definition of the integrated $\tau_{\rm th}$ surfaces for T32L5.2, shown as the cumulative area fraction vs. thermalization optical depth (see Equation (2)). The line styles indicate the locations of the terminations of the optical depth integrals, stopping at the tops and bottoms of the layer cells, $x_{\tau_{\rm th}}$, shown by the dashed and solid lines, respectively. The vertical dotted lines mark the value of $\tau_{\rm thresh}$, and the colors identify different choices of $\tau_{\rm th}$ for the iso-τ surfaces ($\tau_{\rm th} = 1$ and $\tau_{\rm th} = 5$ being green and blue, respectively).

The spatial variety of the integrated $\tau_{\rm th}$ along the bottom of the TCs is shown in the top panel of Figure 4, which also depicts the r, T, $v_{\rm r}$, and $v_\perp$ (in vertical order) of the TCs for T32L5.2 and T19L6.4. Several distinct plumes can be seen, as the radial extent varies in the second-from-top panels, with two plumes extending an additional stellar radius in T19L6.4. The plume structure is also emphasized by the contrasts in radial

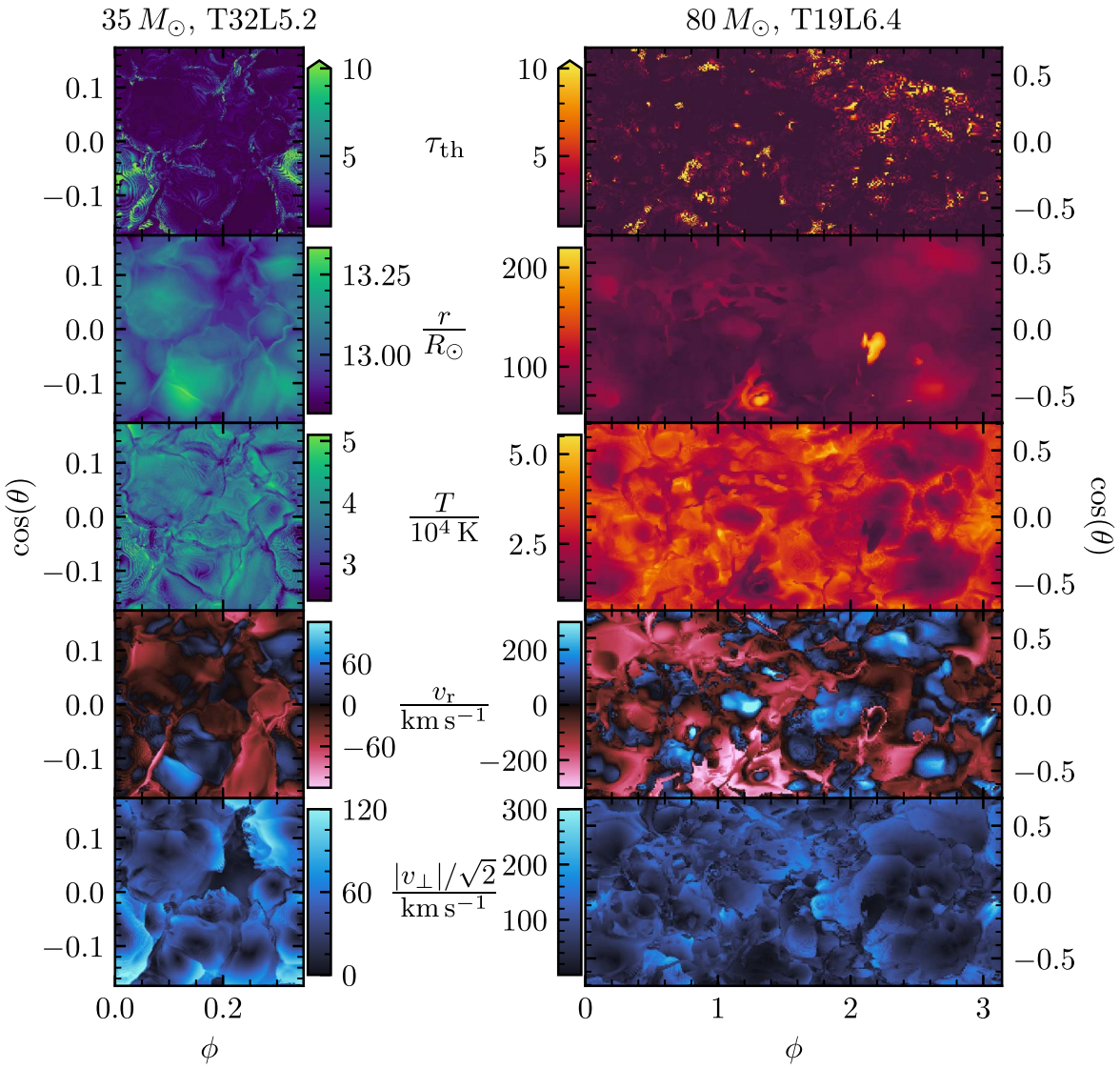

Figure 4. Properties of the models T32L5.2 (left) and T19L6.4 (right) along the integrated $\tau_{\rm th} = 1$ surface, from the outer boundary of the simulation domain along radial lines of sight. The thermalization optical depths integrated through the cell ($\tau_{\rm th}$), the radius (r), the temperature, (T), the radial velocity ($v_{\rm r}$), and the tangential velocity magnitude ($|v_\perp|/\sqrt{2} = \sqrt{0.5(v_\theta^2 + v_\phi^2)}$) are plotted from top to bottom. The colorbars of the tangential velocity panels are identical to the positive (outward velocity) halves of the radial velocity panels.

velocity, shown in the second-from-bottom panels. The temperature is more or less stratified, with higher material being cooler than that beneath it, though the variety in temperature is relatively small. Looking at T along this surface in T19L6.4, it may be surprising that we find $T_{\rm eff} = 19{,}000$ K, when visually the average temperature along $\tau_{\rm th} = 1$ appears closer to 30,000 K. This is due to $\tau_{\rm th} = 1$ being below the $\tau = 1$ surface, and because the stated $T_{\rm eff}$ is defined by the location where $\langle\tau\rangle = 1$. The cool dense plumes shift this photospheric definition farther out, reducing the calculated $T_{\rm eff}$. If, instead, we use the photospheric definition of $\langle F_{\rm r}\rangle = \sigma\langle T\rangle^4$, we find better agreement (see $T_{\rm eff,F_r}$ in Table 1). These are just two choices of a photosphere, which are typically consistent in 1D modeling, but have drastic differences in 3D models, implying that more care is needed when defining the emission surface of a 3D clumpy envelope.

In LTE, T, ρ, and the chemical composition determine which lines are excited, while the velocities determine their resulting profiles. As T varies along the last emitting region, different regions could be exciting different lines. Furthermore, as the temperature is relatively smooth along fixed (θ, ϕ), this implies that spectral lines are emitted from a relatively broad region, rather than a single radial location. We also expect significant spectral broadening, as both the radial and tangential components of the velocity field are strong ($\gtrsim$100 km s^{-1}), with large plumes circulating up and down, with substantial tangential motions. These plumes are a scale height in size, setting the scale of the velocity field, which, at $\tau = 1$, implies a photon mean free path comparable to the turbulent scale. As the boundary between micro- and macroturbulent velocities is often identified by the coherence length of the velocity field being larger or smaller than the emitting region, we expect this complex velocity structure to contribute to both the micro- and macroturbulent broadening. Both the extended emission region and the turbulent velocity field significantly impact the photospheric lines and motivate our spectroscopic analysis.

3. Post-processing Using MC Methods

The required computational resources needed for frequency-dependent 3D RHD would be more prohibitively expensive than those for gray 3D RHD models. Instead, a more productive approach to predicting the observables is to post-process the 3D RHD models with a frequency-dependent radiation transport code. To this end, we modify the MC radiation transport framework SEDONA, which was originally developed for synthesizing photometric and spectral observations from stellar transients (Kasen et al. 2006).

MCPs, each representing many actual photons, are propagated through a user-defined medium, interacting with the matter before reaching the outer boundary of the simulation domain, where they are collected and binned to yield a synthetic spectrum. SEDONA computes frequency-dependent opacities for each zone, by including the contributions from electron scattering, bound–free/photoionization cross sections (Verner et al. 1993), free–free absorption (Gronenschild & Mewe 1978), as well as bound–bound/line opacity (Kurucz & Bell 1995; Verner et al. 1996). By default, SEDONA incorporates the line opacity, via a line expansion formalism that is suitable for the steep velocity gradients of supernovae (Eastman & Pinto 1993). In our work, we remove the line expansion formalism, while aggregating the contributions from individual lines, to build the opacity table for radiation transport, using atomic data from the CMFGEN database (Hillier 2012). We adopt solar abundances for both the ATHENA++ and SEDONA models. We assume LTE in SEDONA, to compute the ionization fractions and level populations of each atomic species. Performing single-zone non-LTE validation calculations at similar T, ρ combinations using our 3D models confirms that the level populations that give rise to the photospheric lines investigated in this work are not affected by non-LTE effects by more than 20%, even at the extremes of the atmospheric conditions. However, other level populations can deviate by an order of magnitude, so further care will be needed in expanding this work beyond the chosen lines. As SEDONA has been used for numerous frequency-dependent applications (e.g., Kozyreva et al. 2020; Tsang et al. 2020), the radiation transport methodology has been extensively tested and compared with other codes, so we focus on describing our substantial modifications that extend SEDONA's application realm to the surfaces of massive stars.

In SEDONA, the MCPs are propagated in Cartesian coordinates, allowing for simple particle propagation during the transport step as well as the flexibility of utilizing different grid geometries. As the ATHENA++ models use a spherical wedge geometry, which SEDONA lacked, the first modification includes a 3D spherical wedge geometry with periodic boundary conditions. The full-sphere geometry is modified to have finite angular extents with periodic boundary conditions in both θ and ϕ. Specifically, when the MCPs encounter a θ or ϕ boundary, their (θ, ϕ) positions are set such that the MCPs are just inside the opposite boundary (e.g., ($\theta_{\rm max}$, $\phi_{\rm min}$) $\rightarrow$ ($\theta_{\rm min} + \delta$, $\phi_{\rm max} - \delta$), where δ is small), whereas their spherical velocity components ($v_{\rm r}$, v_θ, and v_ϕ) are unchanged.

The second major modification deals with the large radial extent of the photosphere prevalent in the 3D models. As shown in Figure 4, and discussed in Section 2, the ATHENA++ envelope models have very clumpy surfaces, with sharp transitions in optical thickness. Thus, if particles are initialized at a constant radius, where all lines of sight have $\tau > 1$, some photons would be propagating through cells with $\tau_{\rm cell} > 100$, causing the MC transport to be computationally prohibitive. Moreover, the radiation transport in such high-$\tau_{\rm cell}$ regions is tedious, as the particles are purely diffusive and it has already been well characterized by the ATHENA++ gray model. Thus, instead of using a constant radius, we define a custom emitting region (CER) using the TCs described above, which avoids the unnecessary computational costs of following long particle histories in diffusive zones.

We initialize the CER using the TCs defined by $\tau_{\rm th}$ surfaces similar to those plotted in Figure 4. The main difference is that a higher $\tau_{\rm th}$ should be chosen to ensure thermalization before the MCPs reach optically thin material and escape. Through testing, we found no noticeable difference between $\tau_{\rm th} = 5$ and $\tau_{\rm th} = 10$, so used the $\tau_{\rm th} = 5$ surface for the CER in our models. The comoving radiative flux, contained in the input model, then defines the initial energy emitted from the desired grid zones of the CER. The user then defines the total number of particles to be emitted, which are evenly divided among the emitting zones.

More specifically, the MCPs are randomly generated along the faces through which the radiative flux leaves the cells. The particles are then isotropically emitted along the direction normal to the cell faces. To validate this initialization approach, an alternate method was developed, in which the MCPs are placed at the center of each zone and isotropically emitted along the direction of the comoving radiative flux, to ensure sufficient angular sampling of the radiation field. In this work, as the particles are only emitted in the optically thick diffusive regime, both initialization methods produce the same results. As ATHENA++ is an Eulerian code, with cell-centered values, using the first prescription is technically more correct for propagation. However, as this forces the MCPs to propagate though half the optically thick zone, it is noticeably slower than the face emission technique. Thus, for this work, we use the face emission method, as the results have proven to be identical.

3.1. Verifying Novel Modifications: Comparing Gray Radiation Transport

The major modifications to SEDONA are first tested using a gray radiation transport setup. Using ρ, T, and the gray $\kappa_{\rm Ross}$ from the T32L5.2 ATHENA++ model as inputs, a CER is initialized with the $\tau_{\rm th} = 5$ TCs using the comoving radiative flux from ATHENA++. SEDONA then initializes particles and propagates them through the $\tau_{\rm th} < 5$ region of the model, tallying the flux through this region, while keeping $T_{\rm gas}$ and ρ fixed. Figure 5 compares the spherical components of the comoving flux above the CER between SEDONA and ATHENA ++. The locations of the angular slices are chosen to highlight the agreement across the high dynamic range of the radiative flux. The large-scale structures in the radiative flux are well reproduced, and the overall radiation transport is consistent through the models.

ATHENA++ appears to have some smaller-scale structures that are smoothed in the SEDONA recreation. These differences are amplified when comparing the θ and ϕ components of the flux, as they are an order of magnitude less than the radial component. Regardless of the number of MCPs that are used in SEDONA, the diffusive nature of the radiative flux (highlighted in the ϕ slice of the θ component of the flux in Figure 5) remains, implying that the isotropic emission used in the CER

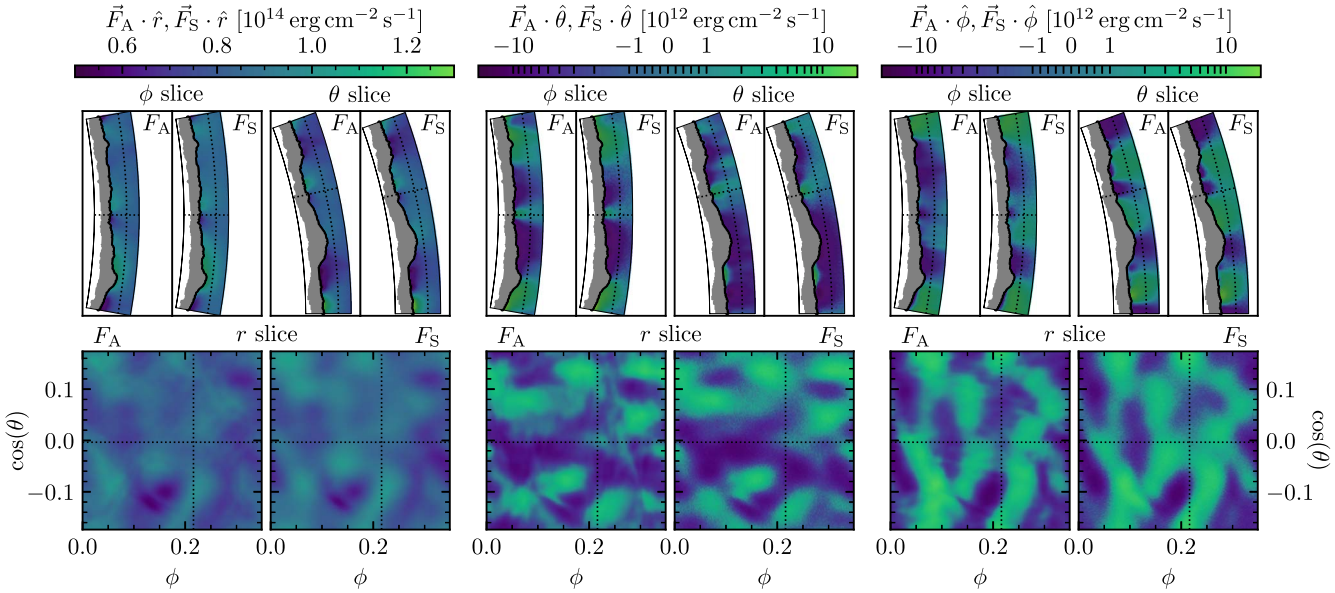

Figure 5. Side-by-side comparison of the radiative flux in the gray radiation transport of ATHENA++, $\boldsymbol{F}_A$, and of SEDONA, $\boldsymbol{F}_S$, through the same snapshot from T32L5.2. The three components of the flux, in spherical coordinates, are directly compared: radial, longitudinal, and latitudinal, from left to right. Each component is compared over three slices: one at constant longitude (ϕ slice), another at constant latitude (θ slice), and one at constant radius (r slice). The gray shaded region shows the extent of the CER from the full wedge of the SEDONA run, with the black line highlighting the outermost extent at $\tau_{\rm th} \approx 5$. The outer extent of the computational domain is well beyond the photosphere. The dotted black lines depict where the slices intersect. All panels have unity aspect ratios.

method is likely to be the culprit. Fortunately, the agreement between the gray radiation transport of SEDONA and ATHENA++ is strong, and it does not affect the generation of synthetic spectra, making it suitable for this work.

It is also interesting to note that the radiation flux at $\tau \geqslant 1$ is not purely radial. The large-scale plume structures generate tangential temperature gradients, producing diffusive radiative flux in the θ and ϕ directions. This can be seen in the middle and right collections of panels in Figure 5, where the two components are nonzero, even at the emitting layer, at $\tau \approx 5$. These tangential temperature gradients lead to a ≈10% deviation from the purely radial gradient used in deriving the limb darkening mechanisms at stellar surfaces. It is unclear how the nonradial temperature gradient will affect limb darkening, but we would not expect them to be the same, and further investigation is warranted.

4. Synthesizing Spectra via Post-processing

Performing full frequency-dependent transport through a 3D envelope model, even when post-processing a simulation snapshot, is computationally expensive. The frequency-dependent opacity, κ_ν, must be calculated for each cell individually, based on the local T, ρ, and chemical composition. Furthermore, a sufficient frequency resolution is needed to resolve the line widths in the comoving frame, the lower limit of which is set by the thermal velocities of ionic species, $v_{\rm therm} \approx \sqrt{2kT/Am_{\rm p}}$, where A is the atomic number. For our models, $v_{\rm therm} \sim 1$–10 km s^{-1}, resulting in a requirement of $\delta\nu/\nu \sim 10^{-6}$. Enforcing the required frequency resolution across a full stellar spectrum becomes extremely memory intensive for the spatial resolution of our models. Additionally, as the κ_ν near the line centers greatly exceeds the opacity of the adjacent continuum, the MCPs tend to be reemitted near the opacity peaks of spectral lines, increasing the true computational costs over the $\tau_{\rm th}$ estimate.

Therefore, in order to demonstrate the utility of proper spectral modeling, we focus on single isolated spectral lines. We choose known photospheric lines (O III at 5594 Å and He I at 6680 Å) that are isolated from neighboring lines, to ensure that the lines do not merge and enough continuum is present for correct normalization. Additionally, we choose lines whose κ_ν peaks rise to at least 10 times the continuum opacity at each model's photospheric T and ρ, to ensure similar reasonable run times. We constrain $\Delta\lambda > 4(1 + v_{\tau=1}/c) * \lambda_0$, where $v_{\tau=1}$ is the maximum photospheric velocity, c is the speed of light, and λ_0 is the line center.

At the line centers, κ_ν are much larger than their adjacent continuum, which is typically also larger than the gray Rosseland mean opacity for a given T and ρ. Thus, the calculation of the gray $\tau_{\rm th}$ surface using the Rosseland mean opacities will be deeper than that for the frequency-dependent emitting surface. Using the gray emitting surface will result in longer computation times, as MCPs have to travel through optically thick cells with long particle histories. However, as we are using an MC approach, we can increase the calculation efficiency by identifying the region of last thermalization for the MCPs and using that as a CER. We determine the layer of last thermalization by initializing the MCPs at the outer boundary of the simulation domain, then propagating them radially inward along constant (θ, ϕ). Recording the cells where each MCP first experiences a thermalization event, which is typically a line absorption event, as $\kappa_\nu \gg \kappa_{\rm gray}$, provides a good localization to the expected emission region. Along radial rays with constant (θ, ϕ), the cells below the deepest cells in which a thermalization event occurs are used as the CER for spectral synthesis, to ensure that all MCPs experience at least one thermalization event before escaping.

To further improve the computing time, we also reduced the angular dimensionality of the 3D RHD models used as inputs to the spectral synthesis calculation by a factor of 4 (e.g., $256 \times 256 \rightarrow 64 \times 64$), by averaging the quantities in each cell. Volume-weighted averages were used for ρ and the radiative

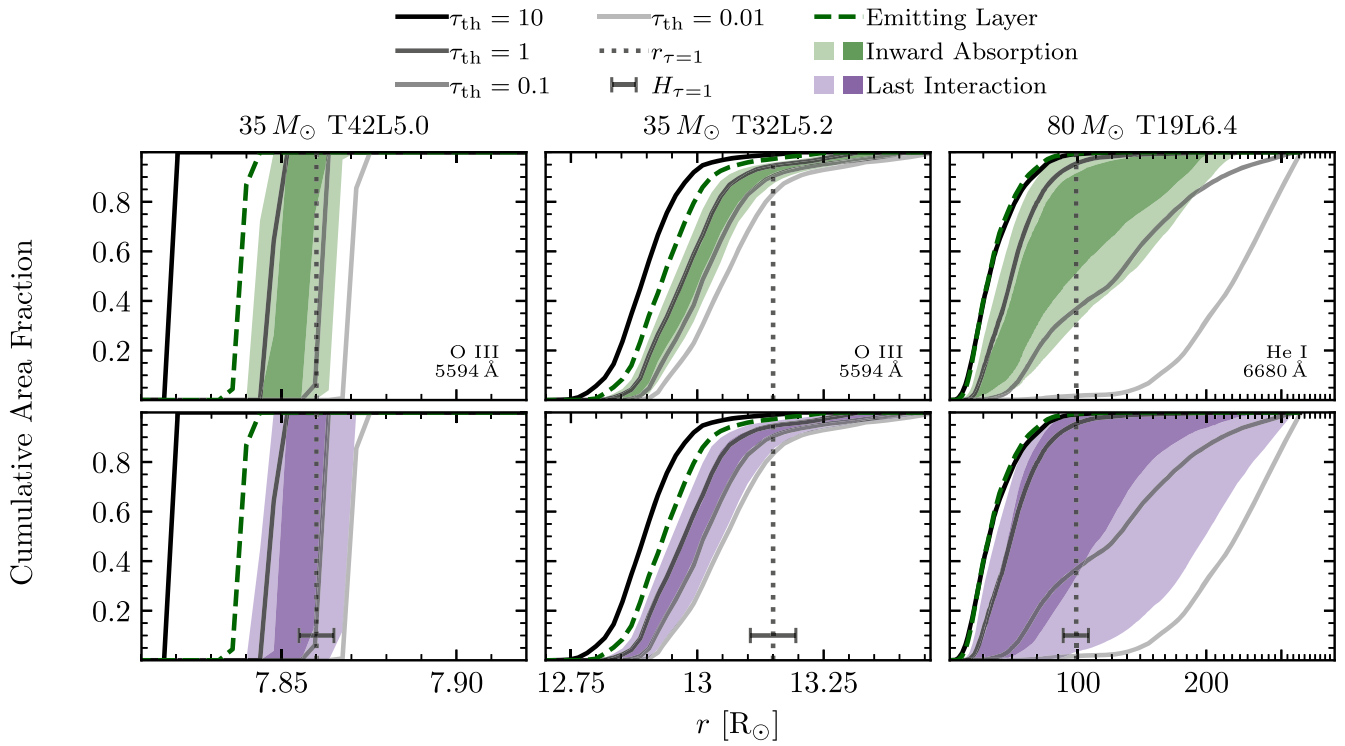

Figure 6. Comparison of the $\tau_{\rm th} = 10$, 1, 0.1, and 0.01 surfaces (solid black lines, from opaque to transparent, respectively) with the regions where MCPs are first thermalized when propagating radially inward (shaded green regions in the top panels) and the regions where the MCPs last thermalized when propagating outward (shaded purple regions in the bottom panels) in our 3D models. Each column is for different 3D models—T42L5.0, T32L5.2, and T19L6.4 (from left to right, respectively)—showing individual spectral lines: O III 5594 Å for T42L5.0 and T32L5.2, and He I 6680 Å for T19L6.4. The two shades of the shaded regions signify the areas where 68% and 95% (lighter and darker, respectively) of the MCPs interact. The dashed green line shows the farthest inward location that the inwardly propagating MCPs reach, which is also used as the emitting layer for the outward-moving MCPs. The vertical dotted gray line shows the spherically averaged photosphere, $r_{\tau=1}$, and the gray scale bar shows the spherically averaged scale height at that radius, $H_{\tau=1}$.

energy density, $E_{\rm r} \propto T^4$, while the velocities and opacities were mass-weighted and all the fluxes were weighted by both opacity and mass. The weightings of the fluxes were chosen due to the significant correlations between ρ, κ, and $F_{\rm r}$, which need to be accounted for in the average (see Schultz et al. 2020). In preliminary testing, this rebinning had no effect on the resulting spectral line profiles, when compared to the full resolution. Combining the lower resolution with the isolation of a single line allowed a full spectral profile of T19L6.4 to be modeled with 200 frequency bins, over 32 hr on a single compute node with 40 cores. This computational efficiency is important for our spectral synthesis code, as it allows others to use the methodology on easily attainable resources.

The top panels of Figure 6 compare the thermalization locations resulting from inwardly propagating the MCPs to several integrated $\tau_{\rm th}$ surfaces for each model. Despite being classified as photospheric lines, the majority of the observed thermalization locations lie outside the $\tau_{\rm th} = 1$ surface and reach out to $\tau_{\rm th} \lesssim 0.1$. Using the inward MCPs to define the CER, the MCPs are propagated outward, as detailed in Section 3. The location of last thermalization for each MCP before it leaves the outer boundary is also recorded, and the distributions of these locations are shown by the purple shaded regions in the bottom panels of Figure 6. The spatial locations of the green and purple distributions match well, validating the inward propagation method that is used to approximate the region of last thermalization and ensuring that each MCP experiences at least one thermalization event before escaping.

Figure 6 also highlights the differences in surface variability between the different models. In T42L5.0, where the turbulence is subsonic, both the $\tau_{\rm th}$ surfaces and the two shaded regions appear steplike in shape, implying that the constant radius approximation is acceptable in these cases. Comparing T42L5.0 to T32L5.2 and T19L6.4, we see far more extended $\tau_{\rm th}$ surfaces and emitting regions, with the more turbulent T19L6.4 spanning nearly an order of magnitude more in radius. Additionally, although the shaded regions do not lie on single $\tau_{\rm th}$ surfaces, their trends do match those of the $\tau_{\rm th}$ surfaces, implying that the assumption of an emission layer with a finite depth is justified, as $\Delta\rho/\rho \ll 1$.

The regions of last interaction in all three models can be compared to the local pressure scale height, $H_{\tau=1}$, to estimate the relative importance of micro- and macroturbulence in the spectral broadening. In T42L5.0, the emitting region spans two local pressure scale heights, which is consistent with the small degree of ρ fluctuations, as shown in Figure 1. Similarly, the last interaction region in T32L5.2 only spans a single local pressure scale height for most of the surface area, yet it covers a much larger radial extent, similar to the $\tau_{\rm th}$ surface shown in Figure 4. The variety of the radial locations of the emitting regions causes the MCPs to thermalize at different T, ρ, $v_{\rm r}$, and $v_\perp$, which should manifest as macroturbulent broadening in the spectral line profiles. The most turbulent model, T19L6.4, displays an emitting region that spans many $H_{\tau=1}$, covering nearly twice the stellar radius in extent. The turbulent broadening should be dominated by individual plume dynamics, as they are expelled from the stellar surface.

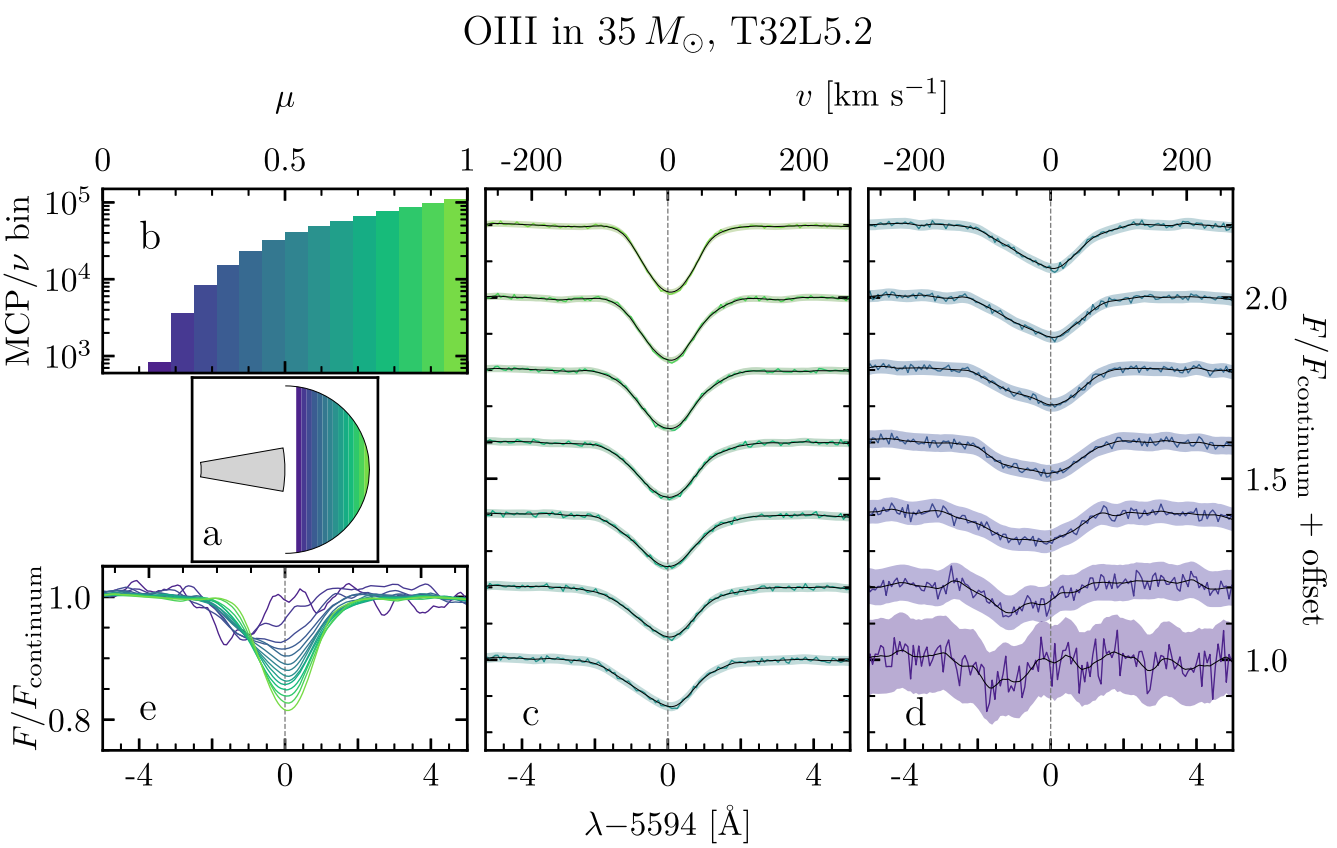

Figure 7. Analysis of the viewing angle dependence in the O III line of T32L5.2. (a) Schematic showing the simulation domain in gray, with the colored areas showing the different $\mu \equiv \cos(\theta)$ bins relative to the pole of the capturing surface. In all panels, the colors represent the given μ bins shown in this schematic. (b) Histogram of the median number of MCPs per frequency bin in each μ bin. (c) and (d) Normalized spectral lines, including a vertical offset. The colored lines are the raw synthesized spectra from the different μ bins shown in (a), which are then smoothed with a Gaussian kernel (black lines). The colored regions show the 3σ error from the smoothed spectral line. (e) Overlay of all the smoothed, normalized spectral lines from (c) and (d).

5. Variety in Synthetic Spectra of 3D Envelope Models

To model the individual spectral profiles, selected using the criteria outlined in Section 4, we use a frequency range that is centered on the line center and extends to include three Doppler widths associated with the maximum surface velocity on either side. Mathematically, the frequencies range from $\nu \in [\nu_0 - 3v_{\rm max}/c,\ \nu_0 + 3v_{\rm max}/c]$, where ν_0 is the frequency at the line center and $v_{\rm max}$ is the maximum magnitude of $v_{{\rm r},\tau=1}$ and $v_{\perp,\tau=1}$ for each model in Table 1. To ensure adequate sampling of the spectral lines, we linearly divide the frequency range into 200 frequency bins, ensuring that the turbulent broadening will be captured by at least 10 frequency bins on either side of the line center.

5.1. Viewing Angle Dependence

To investigate the spectral lines as a function of viewing angle, we divide the outgoing MCPs into 17 $\mu \equiv \cos(\theta)$ bins, where θ is the angle between the propagation direction of an escaping MCP and the pole. The pole of each model is defined as the radial unit vector at $\theta = (\theta_{\rm min} + \theta_{\rm max})/2$ and $\phi = (\phi_{\rm min} + \phi_{\rm max})/2$. Panel (a) of Figure 7 shows a schematic of the μ discretization, with color-coded bins, which are evenly spaced in μ to standardize the surface area of each bin. The two most tangential bins are omitted from this analysis (not shown in Figure 7), as most of the flux is radial ($\boldsymbol{F}_{\rm r} \approx F_{\rm r}\hat{r}$), and thus few MCPs leave the domain at these small μ. Due to the limited number of MCPs in these μ bins, we omit them from this analysis.

The median number of escaping MCPs per frequency bin of the outgoing radiation as a function of μ is shown in panel (b) of Figure 7. The $\mu = 1$ bin receives two orders of magnitude more MCPs than the most tangential bin, as a result of the radial component of the flux surpassing the tangential components by an order of magnitude. This reduction in particle numbers is also responsible for the increase in spectral noise when going from $\mu = 1$ to $\mu = 0.125$ (from the green to purple lines in panels (c) and (d) of Figure 7). This noise is quantified assuming Poisson statistics and using $\sigma = \epsilon\sqrt{N}$, where ϵ is the average flux carried by each MCP and N is the number of MCPs in each ν bin. The shaded regions around each spectral line in panels (c) and (d) of Figure 7 show the 3σ extent above and below the smoothed spectral line shapes (the black lines). The smoothed profiles utilize a Gaussian kernel of 0.5–1 Å, with $\sigma_{\rm smooth} \approx 0.1$ Å. Panel (e) overlays all the smoothed spectral line profiles, for comparison.

The μ dependence of the spectral lines from all three models for two temporal snapshots more than a day apart can be seen in Figure 8. The temporal separation between the snapshots is much longer than the eddy turnover times at the Fe opacity peak (1–4 hr), so the surface dynamics of these snapshots should be uncorrelated. Specifically, these times were chosen to display some of the maximally different spectral profiles that appear in our models. The three models show very different

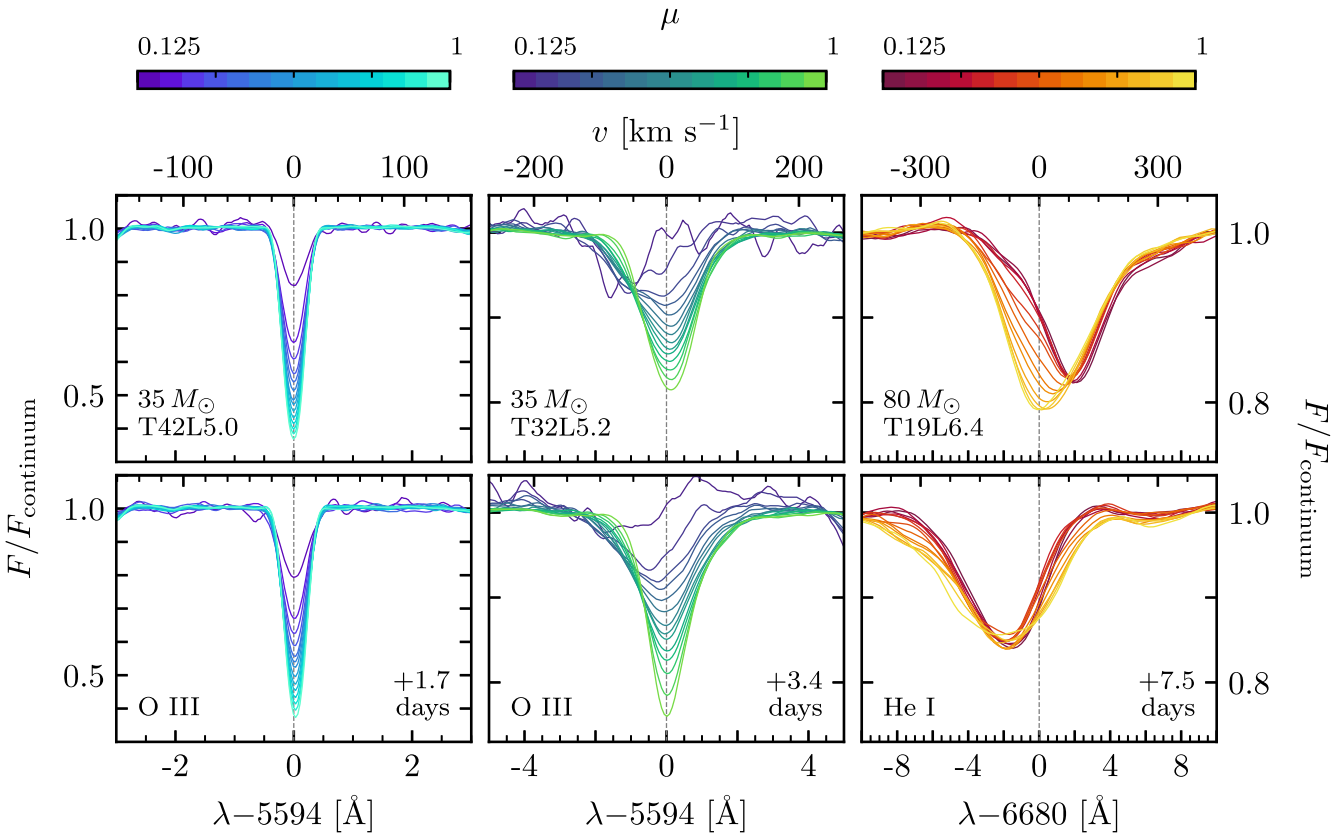

Figure 8. Comparison of the viewing angle (colors) and temporal (top vs. bottom panels) dependences of chosen spectral lines in T42L5.0, T32L5.2, and T19L6.4 (from left to right). Each panel is equivalent to panel (e) in Figure 7.

spectral line shapes, as well as very different temporal line profile variability.

For the models T42L5.0 and T32L5.2, the depth of each line appears to change as a function of μ. The line profiles at lower μ, generated from MCPs with more tangential trajectories, appear to have shallower depths, and thus smaller equivalent widths. These decreases in the μ dependence of the absorption depth are likely due to a limb-darkening-like effect. The MCPs collected in the lower-μ bins are emitted from higher up in the model atmosphere, where the line excitation is weaker, resulting in shallower lines. This is further confirmed by the lack of such μ dependence in T19L6.4, which covers much more of the stellar surface, allowing every μ bin to be dominated by the radial component of the flux, thus having more consistent line depths. In T32L5.2, the low-μ trajectories are also broadened and less symmetric, as the emitting region is more complex, with dynamic topography and velocity fields arising from the stronger turbulent plume motions. The additional broadening is a result of $v_{\perp,\tau=1} > v_{\mathrm{r},\tau=1}$ (see Table 1), which broadens the more tangential trajectories of the low-μ bins. The asymmetry originates from the development of the plume structures. As the individual plumes are now separated from one another, their bulk motion affects the spectral line shape by Doppler shifting parts of the profiles. As the individual plumes do not cover a large area fraction, most of the effects cancel out, resulting in the high-μ peaks being nearly centered on the line center. However, individual plumes with large tangential velocities cause slight shifts away from the line center in low-μ profiles.

The μ dependence is starkly different in T19L6.4 as compared to the previous two models. This stellar model is more radially extended, resulting in a larger scale height and therefore larger plumes. The motions of individual plumes, which cover a significant fraction of the stellar surface, significantly alter the spectral profiles. For example, the redshift seen in the dark red lines, the low-μ profiles, in the upper right panel of Figure 8, are the result of plumes that had previously been launched from the stellar surface falling back down. In contrast, the central regions (the yellow lines in the same panel) do not exhibit a dominant plume motion and thus show no bulk Doppler shift. In the second snapshot (the bottom right panel), all the μ profiles are blueshifted, as several uncorrelated plumes are being launched in different directions. The change of slope in the upper panel near $v \approx 300$ km s^{-1} arises from a neighboring spectral line, which is four times weaker than the main He I line and does not impact the broadening of the line investigated here. The temporal changes in spectral shape should be observable in some of the models, and they are explored further in the next section, when more realistic synthetic profiles are generated.

5.2. Synthetic Spectral Profiles

Our 3D RHD models only cover a patch of the stellar surface, and in T42L5.0 and T32L5.2 especially, the small patch size may affect the resulting spectral shapes. One way of producing more realistic spectral profiles would involve tessellating uncorrelated simulation domains together to generate a hemispherical model. Post-processing this hemispherical model would produce more realistic spectral profiles. The computational memory overhead of such an analysis would depend on the atmospheric H/r value, and for our

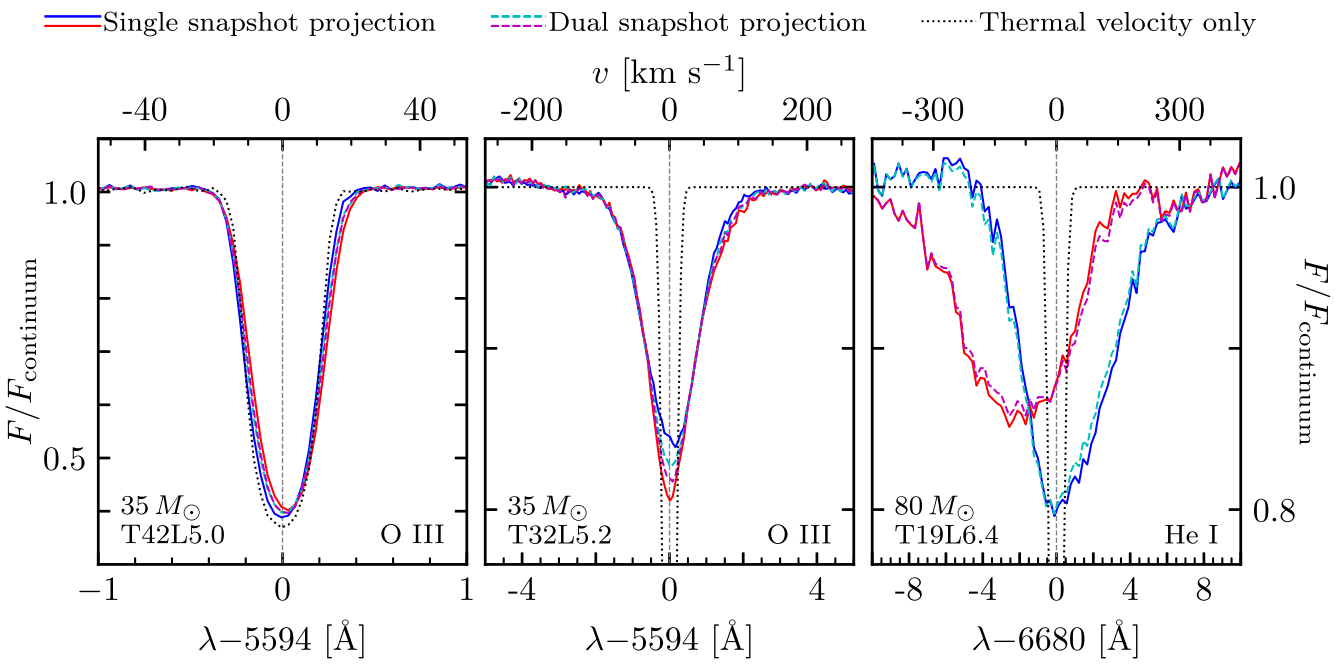

Figure 9. Synthetic spectral lines generated from combining the μ-dependent components shown in Figure 8. Three combinations were chosen: the solid red and blue lines show single-snapshot estimates; the dashed cyan and magenta lines show when alternating μ bins were used, from both of the temporal snapshots; and the dotted black lines show a single snapshot with only the thermal velocity used.

current models it would be computationally challenging, but this may be explored in future work. Another solution would be to use the viewing angle dependence to perform a weighted average of uncorrelated snapshots. In this subsection, we present approximate spectral profiles, based on combining the μ-binned spectral lines from the temporally uncorrelated snapshots shown in Figure 8. Because we are only using two snapshots, we refrain from performing detailed quantitative spectral line analysis for the synthesized profiles. However, an approximate quantitative analysis of the different broadening mechanisms is provided below.

As the narrow models (T42L5.0 and T32L5.2) are small (covering only a 50th of the stellar surface), we perform a weighted sum of the spectral flux from individual snapshots, using each μ bin's projected area on the stellar disk as the weights. Dividing by the mean of the resulting continuum produces the solid red and blue lines in the left and center panels of Figure 9. The same procedure is performed for T19L6.4, but as the original angular coverage is much larger (covering ≈80% of the stellar disk), the $\mu = 1$ bin is taken for the whole area of the simulation domain and is weighted by its projected area on the stellar disk. The remaining area of the stellar disk is added to the weighted sum, using the same procedure as above, and the normalized spectral profiles are shown by the solid red and blue lines in the right panel of Figure 9. In an attempt to represent what an uncorrelated surface may look like, we perform a weighted average, using alternating μ bins from the two available snapshots. As the dashed lines in Figure 9 show, the similar colors represent which snapshot's $\mu = 1$ bin was used (e.g., the dashed cyan line used the same central bin as the solid blue line). To investigate how the bulk velocity field of the cells affects the spectral lines, additional calculations were run, with all the cell velocities set to zero, to generate spectral profiles resulting only from thermal broadening (shown by the dotted black lines). Ideally, we would have used many temporally uncorrelated snapshots in the projection, but as our computational resources were limited, we leave this for a future exercise.

Taking these simple synthetic spectral profiles as truth, we predict that all three models should show some temporal variability. The variability in T42L5.0 would be very challenging to observe, requiring an $R \sim 200{,}000$ spectrometer to measure the slight shift in the line center and a very high signal-to-noise ratio to catch the change in depth of the absorption line. Model T32L5.2 would show signs of variability using only an $R \sim 20{,}000$ spectrograph with a sufficient signal-to-noise ratio to resolve the change in the line shape. The temporal variability of the third model, T19L6.4, should be easy to resolve with many spectrometers. All the small fluctuations present in the colored spectral profiles are due to the Poisson noise from the finite number of MCPs, and are compounded by the fact that only two uncorrelated snapshots were used. If more snapshots and MCPs had been used, we would expect significantly smoother lines. Additionally, the inclusion of more uncorrelated snapshots in the projection process may reduce variability, further constraining the challenge of observing the temporal line variability.

5.3. The Effects of Micro- and Macroturbulence

All three panels of Figure 9 clearly show additional broadening beyond thermal broadening. As there is no rotation in these models, this additional broadening can only be attributed to the impact of the turbulent velocity fields of the envelopes, resulting in ξ and $v_{\rm macro}$. However, it is difficult to determine the individual impacts of ξ or $v_{\rm macro}$ on the broadening without a full quantitative analysis. The simplest distinction would be made by comparing the equivalent widths of the thermal profiles to the full velocity field lines. Should the equivalent width be conserved, $v_{\rm macro}$ would likely be the dominant factor and $\xi < v_{\rm therm}$ (Gray 2005). Conversely, should the equivalent width change, $\xi > v_{\rm therm}$, microturbulence would likely make it hard to quantify $v_{\rm macro}$.

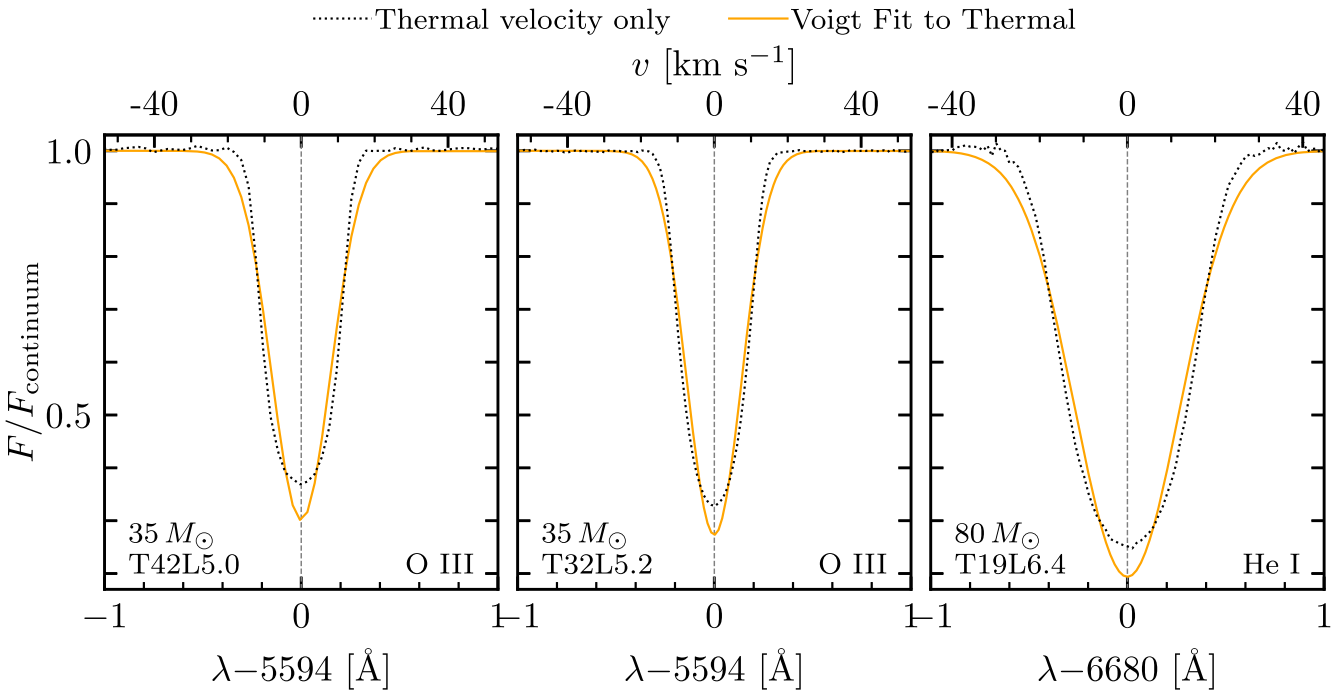

Figure 10. Comparison of thermal spectral lines (dotted black lines from Figure 9) to Voigt profile fits (solid orange lines).

Unfortunately, due to the noise present in the spectral line shapes, it is hard to compare the equivalent widths between the lines without pushing to more MCPs or using more temporally uncorrelated patches. However, comparing the FWHMs of each line can tell us about the dominant velocity. For T42L5.0, the FWHM is $\approx$20 km s^{-1}, which is consistent with thermal broadening, as the FWHM for a Gaussian $\approx 2.4\sigma$. Visually, however, it is clear that the tails of the synthetic profiles in the left panel of Figure 9 are wider than the thermal profile, suggesting the additional presence of macroturbulent broadening. For T32L5.2 the FWHM velocity of $\approx$80 km s^{-1} is comparable to the surface velocities, $v_{\mathrm{r},\tau=1}$ and $v_{\perp,\tau=1}$, in Table 1, suggesting that ξ and v_{macro} are important. Due to the trumpet-like shapes of the profiles, we suspect v_{macro} to be more dominant, although thorough fitting is required to ascertain this. The FWHM velocity of T19L6.4 is $\approx$275 km s^{-1}, which is nearly double the surface velocities in Table 1. This suggests that both ξ and v_{macro} are important in this very turbulent model and that more investigation of the broadening mechanisms is warranted.

Qualitatively, our calculated spectral profile for the O III line in T32L5.2 strongly resembles the observed spectral profiles seen in Simón-Díaz et al. (2014). As our models contain no rotation, the $v \sin i$ values do not agree between our calculations and observations. However, the observed macroturbulence velocities agree quite well with the calculated FWHMs and thus the turbulent velocities in the simulation. Unfortunately, no observations of stars similar to T42L5.0 or T19L6.4 have been carried out. Future spectroscopic surveys (e.g., Bowman et al. 2022) will observe stars that could be directly compared to our other models.

5.4. Thermal Profile Comparison

All the models display noticeable differences from the inclusion of velocity fields. As expected, the cell velocities broaden the profiles and decrease their absorption amplitudes, providing strong evidence for the presence of macroturbulence. To quantify their widths, each thermal profile (dotted black lines) was fit to a Voigt profile (solid orange lines) in Figure 10. As can be seen in the all three panels, , the Voigt profiles do not fit the full thermal profiles very well: the peak is too narrow and the tails are too wide. The discrepancies arise despite the fact that the fit is dominated by the Gaussian component of the Voigt profile, making the peak as wide and the tails as narrow as possible. The lack of a Lorentzian component is not surprising, as SEDONA does not include natural broadening in the calculation of κ_{nu}. However, at the high temperatures of these massive star surfaces, and for our chosen spectral lines, the intrinsic widths should be small compared to the thermal broadening, justifying this assumption.

Despite the shape mismatch between the thermal profiles, the widths of the fits appear to be approximately correct, especially at the FWHM, implying that the standard deviation of the distribution could be used to estimate a thermal velocity with $v_{\mathrm{fit}} = \sigma c/\nu_0$, where ν_0 is the frequency at the line center. However, $v_{\mathrm{fit}} \approx 1.3\, v_{\mathrm{therm}}$, when the thermal velocity is calculated with the temperatures of the emitting region, using $T = T_{\mathrm{eff}}$ (e.g., for T32L5.2: $v_{\mathrm{fit}} = 7.5$ km s^{-1} and $v_{\mathrm{therm}} = 5.7$ km s^{-1}). This difference cannot be explained by microturbulence, as v_{therm} is the only velocity in the calculation of the thermal line profiles. Thus, the discrepancies are either due to the range of T across the emitting region (which vary by $\gtrsim$50% about the mean) or imperfections in the projection method.

6. Conclusion and Future Work

3D spectroscopic analysis of hot massive star surfaces is now possible using the SEDONA MC radiation transport code to post-process 3D RHD LTE ATHENA++ models. The turbulence excited by near-surface convection zones, predominantly those generated from the Fe and He opacity peaks, create large ρ and velocity contrasts that persist through the $\tau = 1$ surface. Because of the inherent plume structure of the turbulent

motions and many-order-of-magnitude density contrasts, the $\tau = 1$ surface is not uniform in radius, but rather spans several pressure scale heights, resulting in factor of 2 variations in T. The T, ρ, and v fluctuations impact the photospheric line broadening, implying that observed spectroscopic broadening could be used to determine the presence and strength of photospheric turbulence.

The viewing angle dependence appears to deviate from classical limb darkening predictions, which is partially due to the small simulation domain, but also due to the tangential temperature gradients that are generated from the dynamic plume structures at the surface. The additionally synthesized spectral lines of our models predict the observable spectral line variability in Hertzsprung gap stars on several-day timescales. Unfortunately, these calculations only use a small simulation domain, and future calculations that mimic the full observed hemisphere of the star are needed for stronger predictions.

Though our calculated line profiles clearly exhibit the large velocities realized in our simulations, it remains to be seen whether they are well represented by the commonly used macroturbulent fitting approach of Gray (2005). For many OB stars, the only inference regarding rotation comes from broad spectral lines that yield a $v \sin i$, based on the assumption that rotation is a dominant broadening mechanism, carried over from analyses of lower-mass stars. Our work here may confound such inferences, as the broadening that we see from turbulence alone may well exceed that from any rotation in many instances, especially stars that are viewed along the rotation axis. Indeed, the lack of reports of low $v \sin i$ with large $v_{\rm macro}$ speaks to this possible challenge to rotational interpretations.

Once spectral lines have been synthesized from hemispherical stellar surfaces, we could use the same methodology as observers to fit rotational and turbulent velocities to the spectral lines. These spectroscopic measurements could then be compared with the fluid velocities in the 3D models. Many spectral lines from single ions could be synthesized and combined to make a curve of growth, allowing ξ to be identified and related to the intrinsic turbulent velocities of the plasma. With the microturbulence quantified, $v_{\rm macro}$ could be identified by calculating the additional broadening needed to fit the spectral line profiles. Last, though the models lack rotation, we could set a bulk rotational velocity distribution to a hemispherical model and begin to probe the interplay between $v \sin i$, ξ, and $v_{\rm macro}$ in massive star surfaces. A better understanding of the interplay between the velocity fields of massive star surfaces could lead to a better theoretical understanding and a more physically motivated explanation of spectral line fitting parameters.

The methodology presented in this work is not specific to our 3D RHD models of hot massive stars. The novel 3D RSG envelope models that have recently been presented in Goldberg et al. (2022) could be analyzed to better understand how larger plume structures affect recent spectroscopic measurements (e.g., Guerço et al. 2022). Though these models were also run with ATHENA++, any 3D model could be used in this method. An additional extension of ATHENA++, using non-gray radiation transport, would also allow the impacts on velocity and density fluctuations to be explored, as well as changes in the temperature gradient, compared to the existing gray models. Additionally, these methods are not specific to optical lines. Other lines could be used, but further care may be needed to ensure that the non-LTE effects do not drastically alter the level populations. With these new methodologies, a comprehensive spectroscopic analysis of massive star surfaces is within reach.

We thank Jared Goldberg, Jorick Vink, Sergio Simón-Díaz, and Sunny Wong for many helpful conversations and comments. This research was supported in part by NASA ATP grant No. ATP-80NSSC88K0725 , the National Science Foundation, through grant No. PHY 17-48958 and ACI-1663688 at the KITP, and the Gordon and Betty Moore Foundation through Grant GBMF5076. Resources supporting this work were also provided by the NASA High-End Computing (HEC) program, through the NASA Advanced Supercomputing (NAS) Division at the Ames Research Center. We acknowledge support from the Center for Scientific Computing from the CNSI, MRL, via NSF MRSEC (DMR-1720256) and NSF CNS-1725797. The Flatiron Institute is supported by the Simons Foundation.

ORCID iDs

William C. Schultz https://orcid.org/0000-0003-1796-9849
Benny T.-H. Tsang https://orcid.org/0000-0002-6543-2993
Lars Bildsten https://orcid.org/0000-0001-8038-6836
Yan-Fei Jiang (姜燕飞) https://orcid.org/0000-0002-2624-3399

References

Aerts, C., & Rogers, T. M. 2015, ApJL, 806, L33
Bowman, D. M., Burssens, S., Pedersen, M. G., et al. 2019, NatAs, 3, 760
Bowman, D. M., Vandenbussche, B., Sana, H., et al. 2022, arXiv:2208.01533
Burssens, S., Simón-Díaz, S., Bowman, D. M., et al. 2020, A&A, 639, A81
Cantiello, M., Lecoanet, D., Jermyn, A. S., & Grassitelli, L. 2021, ApJ, 915, 112
Chiavassa, A., Pasquato, E., Jorissen, A., et al. 2011, A&A, 528, A120
Chiavassa, A., Plez, B., Josselin, E., & Freytag, B. 2009, A&A, 506, 1351
Dravins, D., Ludwig, H.-G., & Freytag, B. 2021, A&A, 649, A16
Eastman, R. G., & Pinto, P. A. 1993, ApJ, 412, 731
Edelmann, P. V. F., Ratnasingam, R. P., Pedersen, M. G., et al. 2019, ApJ, 876, 4
Freytag, B., & Höfner, S. 2008, A&A, 483, 571
Freytag, B., Steffen, M., & Dorch, B. 2002, AN, 323, 213
Goldberg, J. A., Jiang, Y.-F., & Bildsten, L. 2022, ApJ, 929, 156
Gray, D. F. 2005, The Observation and Analysis of Stellar Photospheres (New York: Cambridge Univ. Press), doi:110.1017/CBO9781316036570
Gronenschild, E. H. B. M., & Mewe, R. 1978, A&AS, 32, 283
Guerço, R., Smith, V. V., Cunha, K., et al. 2022, MNRAS, 516, 2801
Hillier, D. J. 2012, in From Interacting Binaries to Exoplanets: Essential Modeling Tools, ed. M. T. Richards & I. Hubeny, Vol. 282 (Cambridge: Cambridge Univ. Press), 229
Holgado, G., Simón-Díaz, S., Herrero, A., & Barbá, R. H. 2022, A&A, 665, A150
Iglesias, C. A., & Rogers, F. J. 1996, ApJ, 464, 943
Jermyn, A. S., Bauer, E. B., Schwab, J., et al. 2022, arXiv:2208.03651
Jiang, Y.-F. 2021, ApJS, 253, 49
Jiang, Y.-F., Cantiello, M., Bildsten, L., Quataert, E., & Blaes, O. 2015, ApJ, 813, 74
Jiang, Y.-F., Cantiello, M., Bildsten, L., Quataert, E., & Blaes, O. 2017, ApJ, 843, 68
Jiang, Y.-F., Cantiello, M., Bildsten, L., et al. 2018, Natur, 561, 498
Jiang, Y.-F., Stone, J. M., & Davis, S. W. 2012, ApJS, 199, 14
Jiang, Y.-F., Stone, J. M., & Davis, S. W. 2014, ApJS, 213, 7
Kasen, D., Thomas, R. C., & Nugent, P. 2006, ApJ, 651, 366
Kozyreva, A., Shingles, L., Mironov, A., Baklanov, P., & Blinnikov, S. 2020, MNRAS, 499, 4312
Krtička, J., & Feldmeier, A. 2021, A&A, 648, A79
Kurucz, R. L., & Bell, B. 1995, Atomic Line List (Cambridge, MA: Smithsonian Astrophysical Observatory)
Paxton, B., Bildsten, L., Dotter, A., et al. 2011, ApJS, 192, 3
Paxton, B., Cantiello, M., Arras, P., et al. 2013, ApJS, 208, 4

Paxton, B., Marchant, P., Schwab, J., et al. 2015, ApJS, 220, 15
Paxton, B., Schwab, J., Bauer, E. B., et al. 2018, ApJS, 234, 34
Paxton, B., Smolec, R., Schwab, J., et al. 2019, ApJS, 243, 10
Ricker, G. R., Winn, J. N., Vanderspek, R., et al. 2015, JATIS, 1, 014003
Rogers, T. M., Lin, D. N. C., McElwaine, J. N., & Lau, H. H. B. 2013, ApJ, 772, 21
Rybicki, G. B., & Lightman, A. P. 1979, Radiative Processes in Astrophysics (New York: Wiley-VCH)
Santolaya-Rey, A. E., Puls, J., & Herrero, A. 1997, A&A, 323, 488
Schultz, W. C., Bildsten, L., & Jiang, Y.-F. 2020, ApJ, 902, 67
Schultz, W. C., Bildsten, L., & Jiang, Y.-F. 2022, ApJL, 924, L11
Simón-Díaz, S., Aerts, C., Urbaneja, M. A., et al. 2018, A&A, 612, A40
Simón-Díaz, S., Godart, M., Castro, N., et al. 2017, A&A, 597, A22
Simón-Díaz, S., Herrero, A., Sabín-Sanjulián, C., et al. 2014, A&A, 570, L6
Simón-Díaz, S., Herrero, A., Uytterhoeven, K., et al. 2010, ApJL, 720, L174
Stone, J. M., Tomida, K., White, C. J., & Felker, K. G. 2020, ApJS, 249, 4
Tsang, B. T. H., Goldberg, J. A., Bildsten, L., & Kasen, D. 2020, ApJ, 898, 29
Verner, D., Yakovlev, D., Band, I., & Trzhaskovskaya, M. 1993, ADNDT, 55, 233
Verner, D. A., Verner, E. M., & Ferland, G. J. 1996, ADNDT, 64, 1